Optimized Cross-Slot Flow Geometry for Microfluidic Extensional Rheometry

Simon J. Haward, Mónica S. N. Oliveira, Manuel A. Alves, and Gareth H. McKinley

Optimized Cross-Slot Flow Geometry for Microfluidic Extensional Rheometry

Simon J Haward[1,3], Mónica SN Oliveira[2], Manuel A Alves[3] and Gareth H McKinley[1]

[1] *Hatsopoulos Microfluids Laboratory, Department of Mechanical Engineering, Massachusetts Institute of Technology, Cambridge, MA 02139, USA*

[2] *Department of Mechanical and Aerospace Engineering, University of Strathclyde, Glasgow G1 1XJ, United Kingdom*

[3] *Faculdade de Engenharia da Universidade do Porto, Centro de Estudos de Fenómenos de Transporte, Rua Dr. Roberto Frias, 4200-465, Porto, Portugal*

Abstract: A precision-machined cross-slot flow geometry with a shape that has been optimized by numerical simulation of the fluid kinematics is fabricated and used to measure the extensional viscosity of a dilute polymer solution. Full-field birefringence microscopy is used to monitor the evolution and growth of macromolecular anisotropy along the stagnation point streamline, and we observe the formation of a strong and uniform birefringent strand when the dimensionless flow strength exceeds a critical Weissenberg number, $\mathrm{Wi}_{crit} \approx 0.5$. Birefringence and bulk pressure drop measurements provide self-consistent estimates of the planar extensional viscosity of the fluid over a wide range of deformation rates $(26\ \mathrm{s}^{-1} \leq \dot{\varepsilon} \leq 435\ \mathrm{s}^{-1})$ and are also in close agreement with numerical simulations performed using a finitely extensible non-linear elastic (FENE) dumbbell model.

Since its first use in the study of drag-reducing polymer solutions [1], the cross-slot device has played a central role in enhancing our understanding of macromolecular dynamics and non-linear effects in complex fluids undergoing strongly extensional flows [2-4]. The cross-slot geometry consists of perpendicular, bisecting channels with opposing inlets and outlets (half-width H), resulting in a flow field with a stagnation point located at the center of symmetry, see Fig. 1(a). At this singular hyperbolic point, the flow velocity is zero but the velocity gradient is finite, and an elongational flow is generated along the streamlines flowing outwards along the x-direction. In polymer solutions, macromolecules become trapped at the stagnation point for (in principle) infinite time and can accumulate significant macromolecular strain provided the velocity gradient ($\dot{\varepsilon}$) exceeds one-half of the relaxation rate ($1/2\lambda$) of the polymer [5, 6], such that the Weissenberg number, $\mathrm{Wi} = \dot{\varepsilon}\lambda > 0.5$. Such behavior has been confirmed in stagnation point flows involving both point-wise birefringence measurements [2, 7] and direct observations of unraveling fluorescently-labeled DNA [3, 8, 9]. Perhaps the most important consequence of the stretching of macromolecules in extensional flows is the associated non-linear increase in the tensile stress difference ($\tau_{xx} - \tau_{yy}$) or equivalently the extensional viscosity ($\eta_E = (\tau_{xx} - \tau_{yy})/\dot{\varepsilon}$), which is important in diverse applications including enhanced oil recovery [10, 11] and turbulent drag reduction [12, 13]. In the cross-slot device the extensional viscosity enhancement is manifested as an excess pressure drop across the geometry, which suggests the potential of such devices as extensional rheometers for complex fluids [14]. However, in traditional cross-slot devices the extension rate is only well-defined at the stagnation point itself and decays rapidly with distance along the flow axes [15]. To circumvent this limitation, Alves [16] proposed a numerical method to design an optimized cross-slot geometry that would result in a constant, homogeneous extension rate along the in- and out-flowing symmetry planes. The resulting shape

2

of the optimal geometry and the strain rate field obtained numerically for Newtonian creeping flow are shown in Fig. 1(b). To illustrate the homogeneity of the strain rate, we plot the velocity gradient $\dot{\varepsilon}_{xx} = \partial v_x / \partial x$ along the outflow direction. For an ideal planar extensional flow with $[v_x, v_y] = [\dot{\varepsilon}x, -\dot{\varepsilon}y] = 0.1U/H[x, -y]$ the deformation rate becomes $\dot{\varepsilon}_{xx} = 0.1U/H$ everywhere. As shown by Fig. 1(b), the ideal kinematics are closely approximated over the central region of the geometry. Near the walls, shearing effects minimize the stretching of fluid elements, but the stagnant concavities at the salient corners of the device help 'self-lubricate' the flow.

Because the viscoelastic stress field τ resulting from these kinematics is a homogeneous extensional deformation, it provides no significant perturbative contribution $\nabla.\tau$ to the equation of motion, and the optimized geometries obtained for a wide range of constitutive equations and Weissenberg numbers are almost identical. Therefore, the kinematics are universally applicable for exploring the extensional response of complex fluids at low Reynolds number (Re). Simulations with a nonlinear dumbbell model utilizing the Chilcott-Rallison closure (FENE-CR) [17] predict the localized extensional stress field in the device shown in Fig. 1(c), with an internal boundary layer in the normal stress difference ($N_1 = \tau_{xx} - \tau_{yy}$) of almost uniform magnitude along the symmetry axis. The advantages of such a device for experimental extensional rheometry are evident: a homogeneous extensional flow field is realized which provides an enhanced excess pressure drop (compared with a conventional cross-slot design) due to the dramatically expanded region of planar elongational flow with constant strain rate. Measurements of flow-induced birefringence in the device can also be averaged along the outflow axis, rather than being monitored only locally at the stagnation point.

In this Letter, we report the fabrication of an Optimized Shape Cross-slot Extensional Rheometer (OSCER, see Fig. 1(d)), with a geometry determined using the numerical

3

optimization scheme outlined by Alves [16]. The OSCER device is shown to impose the numerically-predicted optimized flow field and provides spatially-resolved flow-induced birefringence and global pressure drop data from which self-consistent estimates of the extensional viscosity of a dilute flexible polymer solution are obtained over a wide range of extension rates. The experimental results are also in close quantitative agreement with the predictions of a FENE-CR model.

The device shown in Fig. 1(d) is fabricated from stainless steel by the technique of wire-electrical discharge machining. The inlet and outlet channels are initially parallel (half-width $H = 100$ μm) over a distance of 1.4 mm ($14H$) in the up- and downstream sections. The optimized shape is located over the central 3 mm of the device ($15H$ either side of the stagnation point). The device has a depth of $d = 2.10$ mm (aspect ratio, $\alpha = 10.5$), hence the flow is approximately 2D. The flexible, linear polymer is a high molecular weight poly(ethylene oxide) (PEO, MW = 1 MDa; polydispersity index $M_w/M_n \approx 7$) dissolved to a concentration $c = 0.05$ wt% in 66 wt% aqueous glycerol (solvent viscosity $\eta_s = 0.0129$ Pa s at 25°C). The PEO solution has a low-shear rate viscosity of $\eta = 0.0141$ Pa s which remains almost constant up to shear rates $\dot{\gamma} > 2500$ s^{-1}. The intrinsic viscosity of the PEO solution was calculated to be $[\eta] \approx$ 370 mL g^{-1} [18], indicating an overlap concentration of $c^* = 0.27$ wt% . Hence the fluid is dilute ($c/c^* < 0.2$). The PEO radius of gyration is $R_g \approx 53$ nm, and the equilibrium end-end distance, $\left\langle r_0^2 \right\rangle^{1/2} = \sqrt{6}R_g \approx 129$ nm . The repeat unit mass of 42 Da and length of 0.278 nm [19], defines the contour length of $L_C \approx 6.6$ μm, hence the maximum attainable macromolecular strain is $L = L_C / \left\langle r_0^2 \right\rangle^{1/2} \approx 50$. The relaxation time of the fluid is $\lambda = 6.5$ ms, determined using capillary breakup extensional rheometry (CaBER) [20]. The computed extensibility parameter ($L^2 = 2500$)

4

and measured relaxation time were used in the FENE-CR simulations along with the solvent viscosity (η_s) and the polymer viscosity contribution, $\eta_p = \eta - \eta_s = 0.0012$ Pa s. We define the Reynolds number $\mathrm{Re} = 2\rho U H / \eta$, where the fluid density ρ = 1157 kg m^{-3} and $U = Q/4Hd$ is the "superficial flow velocity" in the upstream and downstream parallel sections of channel, with Q representing the total volumetric flow rate.

In Fig. 2 we quantify the flow field within the OSCER device by performing particle image velocimetry (PIV) on fluid seeded with 1 μm diameter fluorescent tracer particles. At moderate flow rates, Fig. 2(a), the dilute PEO solution exhibits a highly symmetric and Newtonian-like flow field, with circular contours of constant velocity around a central stagnation point. As the flow rate is increased above the coil-stretch transition, Fig. 2(b), the stagnation region becomes elongated along the x-direction and the outflow velocity profile $v_x(y)$ becomes weakly non-monotonic near the exit channels. Such non-monotonic flow profiles can be reproduced numerically by modeling the elastic birefringent strand located along the outflow axis as an internal stress boundary layer within the flow field [21]. Plotting the PIV data for $v_x(x)$, measured along the $y = 0$ axis, illustrates the linearity of the flow velocity (Fig. 2(c)) and the constancy of the extension rate ($\dot{\varepsilon}_{xx} = \partial v_x / \partial x$) for $|x| < 1.5$ mm. At low flow rates, the velocity profile closely matches the Newtonian result (as well as the numerical prediction, not shown). For $|x| > 1.5$ mm the normalized velocity $|v_x/U| \approx 1.6$, as expected for Poiseuille flow of a constant viscosity fluid in a rectangular channel with α = 10.5. Fig. 2(d) shows the velocity gradient ($\dot{\varepsilon}$) measured along the outflow axis for the viscoelastic PEO solution over a range of flow rates, compared with the Newtonian result. The Newtonian velocity gradient increases linearly with flow rate ($\dot{\varepsilon} \approx 1066U$, with U in m s^{-1}), as expected for this optimized geometrical

configuration. For the dilute PEO solution at low flow rates, $\dot{\varepsilon}$ follows the Newtonian trend; however, above the coil-stretch transition the perturbation of the velocity field due to the elastic tensile stresses in the stretching fluid elements results in a weak decrease of the expected strain rate, which is well described as $\dot{\varepsilon} \approx 1066U - 528U^{2.1}$.

The modification of the flow field along the outflowing symmetry axis results from the orientation and stretching of macromolecules in the high velocity gradient. Consequently flow-induced optical anisotropy (birefringence) develops, as shown in Fig. 3(a)-(d) for a range of extension rates. The experiments are performed using a polarizing microscope (ABRIO, CRi Inc.) to measure the point-wise retardation $R(x,y)$ with a spatial resolution of approximately 2 μm/pixel. The retardation is related to the birefringence (Δn) by $R = \int_{-d/2}^{d/2} \Delta n \mathrm{d}z$ (or $R = d\Delta n$, assuming two-dimensional flow). The birefringent elastic strands resulting from the localized macromolecular orientation generate high tensile stress differences and cause an increase in the local extensional viscosity of the fluid. This feeds back on the flow field, causing the reduction in the local flow velocity and modifying the local velocity gradient [7, 21]. In fluids of sufficient elasticity, this flow modification can result in the onset of purely-elastic flow asymmetries, in which the flow field becomes distorted about the stagnation point, leading to spatio-temporally varying kinematics [4, 22, 23].

The variation in the measured retardance along the $x = 0$ axis, Fig. 3(e), shows the extreme localization of stretching along the outflow axis. The localization results from the high strains and extension rates that are required to substantially stretch the flexible macromolecules. Such conditions only arise along streamlines passing very close to the stagnation point, where the residence time is maximal. The full-width at half-maximum of the strands scales with Wi in

6

the form predicted by Becherer et al. [24] (Fig. 3(e), insert). The intensity of the retardance along the lengths of the strands remains essentially constant in x across the entire field of view (Fig. 3(f)). In Fig. 3(g) we plot the intensity of the birefringence measured on the $y = 0$ axis as a function of $\dot{\varepsilon}$, showing the standard deviation as error bars. The birefringence (Δn) first becomes measurable at $\dot{\varepsilon} \approx 100$ s^{-1} and then increases approximately linearly with $\dot{\varepsilon}$. The birefringence can be related to the viscoelastic tensile stress difference in the stretching fluid through the stress-optical rule, $\Delta n = C \Delta \tau$, where C is the stress-optical coefficient. Using an experimentally determined value of $C = 0.44 \times 10^{-9}$ Pa^{-1} (see discussion below) to convert from computed normal stress difference to birefringence, the FENE-CR model accurately predicts the birefringence in the PEO solution (reduced chi-squared value, $\chi_{red}^2 = 0.83$).

The linear increase in birefringence with strain rate is explained by the finite polydispersity of the PEO sample, as successively lower molecular weight fractions of the sample stretch as $\dot{\varepsilon}$ is incremented [2]. The measured birefringence can also be used to estimate the average extension ratio of the PEO chains $\beta = \langle r^2 \rangle^{1/2} / L_C$, where $\langle r^2 \rangle^{1/2}$ is the ensemble-average end-end distance at a given extension rate. We use the model of Treloar [25] to relate the birefringence to the extension ratio through an approximation to the inverse Langevin function. As shown by the insert in Fig. 3(g), the ensemble-average extension ratio first increases at $\mathrm{Wi}_{crit} \approx 0.5$ and rises monotonically to $\beta \approx 0.3$ at $\mathrm{Wi} \approx 2.8$. Numerical simulations and previous stagnation point experiments at low Re (e.g. [3, 7]) suggest that β would continue to increase beyond this value if the extension rate (or Wi) were increased further. However, for this low viscosity aqueous solution, further increases in flow rate result in an inertio-elastic instability ($\mathrm{Re}_{crit} \approx 7.7$, $\mathrm{Wi}_{crit} \approx 2.8$) that distorts the birefringent strand. The corresponding critical value of

the strain rate $\dot{\varepsilon}_{crit}$ could be extended by reducing the characteristic dimension, H. A strongly progressive saturation of the birefringence with strain rate is expected as more of the polymer chains in the molecular weight distribution approach their finite extensibility limit [2, 26].

We evaluate the steady-state extensional viscosity of the dilute PEO test solution using both bulk pressure drop measurements and local birefringence data obtained in the OSCER device. The pressure drop is evaluated in two steps, see Fig. 4(a). The first measurement (ΔP_{total}) is obtained with flow into both opposing inlets and out of both opposing outlets, so that the stagnation point is present and a birefringent strand is formed. Subsequently, one inlet valve and one outlet valve is closed and the pressure drop is measured for steady shearing flow around one corner of the device (ΔP_{shear}). Because of the homogeneity of the extensional flow in this geometry, a simple subtraction allows a first order estimate of the extensional stress carried by the stretching fluid, $\Delta\tau \approx \Delta P_{excess} = \Delta P_{total} - \Delta P_{shear}$. In the insert of Fig. 4(a) we show ΔP_{excess} as a function of $\dot{\varepsilon}$. In Fig. 4(b), we present two measurements of the extensional viscosity and the dimensionless Trouton ratio, $\mathrm{Tr} = \eta_E / \eta$, as a function of $\dot{\varepsilon}$. The hollow circles represent $\eta_E = \Delta P_{excess} / \dot{\varepsilon}$ determined from the bulk pressure drop data and the solid squares represent $\eta_E = \Delta n / C \dot{\varepsilon}$ determined from the local birefringence measurements. The stress-optic coefficient of $C = 0.44 \times 10^{-9}$ Pa^{-1} is found from a linear regression through the origin of the Δn versus ΔP_{excess} plot (Fig. 4(b) insert). This value of C is consistent with values obtained from shear flow experiments with aqueous PEO solutions [27]. For this dilute polymer solution, we measure Trouton ratios of $\mathrm{Tr} \approx 400$ at $\mathrm{Wi} \approx 3$. The solid line in Fig. 4(b) shows the prediction of the FENE-CR model, which is in good agreement with the experiments over a broad range of imposed extension rates.

We have shown that computational optimization techniques can be used to design idealized microfluidic flow geometries for applications in complex fluid rheometry. We optimized the shape of the canonical cross-slot geometry in order to provide a nominally constant extension rate over a greatly extended spatial domain ($\sim 30H$) of the inlet and outlet channels. The optimized kinematic design was confirmed using PIV measurements with a Newtonian solvent and a dilute solution of flexible linear macromolecules. Self-consistent measures of the extensional viscosity of a dilute PEO solution have been extracted from both bulk pressure drop and local birefringence measurements. We have also shown that a non-linear elastic dumbbell model with molecular parameters based directly on the measured viscometric properties and the known chain characteristics of PEO can accurately predict the growth of the extensional viscosity with strain rate. This is the first time that a microfluidic device for complex fluid rheometry has been fully designed using computational optimization tools, and the desired kinematics have been verified experimentally. The OSCER device enables a homogeneous extensional flow field to be applied to dilute and low viscosity polymer solutions, over a far greater range of extensional strain rates than are possible in existing filament stretching and capillary breakup rheometers. Its capabilities can be readily extended by reducing the characteristic channel dimension (to access higher Wi and lower Re). The OSCER offers tremendous potential as the basis for the next generation of cross-slot geometries, not only for measuring the true extensional rheology of complex fluids but also for performing controlled extensional deformations and breakup of droplets [28], vesicles [29] and cells [30].

References

[1] O. Scrivener, C. Berner, R. Cressely, R. Hocquart, R. Sellin, and N.S. Vlachos, J. Non-Newtonian Fluid Mech. **5**, 475 (1979).

[2] J.A. Odell and A. Keller, J. Polym. Sci. Pol. Phys. **24**, 1889 (1986).

[3] T.T. Perkins, D.E. Smith, and S. Chu, Science **276**, 2016 (1997).

[4] P.E. Arratia, C.C. Thomas, J. Diorio, and J.P. Gollub, Phys. Rev. Lett. **96**, 144502 (2006).

[5] P.G. De Gennes, J. Chem. Phys. **60**, 5030 (1974).

[6] R.G. Larson and J.J. Magda, Macromolecules **22**, 3004 (1989).

[7] S.J. Haward, J.A. Odell, Z. Li, and X.-F. Yuan, Rheol. Acta **49**, 633 (2010).

[8] C.M. Schroeder, H.P. Babcock, E.S.G. Shaqfeh, and S. Chu, Science **301**, 1515 (2003).

[9] D.E. Smith and S. Chu, Science **281**, 1335 (1998).

[10] D.F. James and J.H. Saringer, J. Fluid Mech. **97**, 655 (1980).

[11] V. Yamakov and A. Milchev, Phys. Rev. E **56**, 7043 (1997).

[12] J.K. Bhattacharjee and D. Thirumalai, Phys. Rev. Lett. **67**, 196 (1991).

[13] A. Roy, A. Morozov, W. van Saarloos, and R.G. Larson, Phys. Rev. Lett. **97**, 234501 (2006).

[14] J.A. Odell and S.P. Carrington, J. Non-Newtonian Fluid Mech. **137**, 110 (2006).

[15] S.J. Haward, T.J. Ober, M.S.N. Oliveira, M.A. Alves, and G.H. McKinley, Soft Matter **8**, 536 (2012)

[16] M.A. Alves, in The XVth International Congress on Rheology, edited by L.G. Leal, R.H. Colby, and A.J. Giacomin (American Institute of Physics, Monterey, 2008).

[17] M.D. Chilcott and J.M. Rallison, J. Non-Newtonian Fluid Mech. **29**, 381 (1988).

[18] L.E. Rodd, J.J. Cooper-White, D.V. Boger, and G.H. McKinley, J. Non-Newtonian Fluid Mech. **143**, 170 (2007).

[19] H. Tadokoro, *Structure of Crystalline Polymers* (Robert E. Krieger Pub. Co., Malabar, FL, 1990).

[20] S.L. Anna and G.H. McKinley, J. Rheol. **45**, 115 (2001).

[21] O.G. Harlen, J.M. Rallison, and M.D. Chilcott, J. Non-Newtonian Fluid Mech. **34**, 319 (1990).

[22] R.J. Poole, M.A. Alves, and P.J. Oliveira, Phys. Rev. Lett. **99**, 164503 (2007).

[23] S.J. Haward and G.H. McKinley, Phys. Rev. E **85**, 031502 (2012).

[24] P. Becherer, A.N. Morozov, and W. van Saarloos, J. Non-Newtonian Fluid Mech. **153**, 183 (2008).

[25] L.K.G. Treloar, *The Physics of Rubber Elasticity* (Clarendon Press, Oxford, 1975).

[26] P.S. Doyle, E.S.G. Shaqfeh, G.H. McKinley, and S.H. Spiegelberg, J. Non-Newtonian Fluid Mech. **76**, 79 (1998).

[27] Q. Zhang and L.A. Archer, Macromolecules **37**, 1928 (2004).

[28] D.R. Link, S.L. Anna, D.A. Weitz, and H.A. Stone, Phys. Rev. Lett. **92**, 054503 (2004).

[29] V. Kantsler, E. Segre, and V. Steinberg, Phys. Rev. Lett. **101**, 048101 (2008).

[30] D.R. Gossett, H.T.K. Tse, S.A. Lee, Y. Ying, A.G. Lindgren, O.O. Yang, J. Rao, A.T. Clark, and D. Di Carlo, Proc. Nat. Acad. Sci. USA. **109**, 7630 (2012).

FIGURE CAPTIONS

FIG 1. (a) Schematic representation of a cross-slot geometry, showing the coordinate system and characteristic dimension (H). (b) Strain rate field for numerically simulated Newtonian creeping flow in the optimized cross-slot geometry. (c) Computed normal stress difference, $N_1(x,y)$, for flow of a FENE-CR fluid in the optimized geometry at $\dot{\varepsilon} = 400$ s^{-1}. (d) Optical micrograph of the OSCER geometry. The ideal profile obtained by numerical optimization is superimposed in green.

FIG 2. (a) Experimentally measured velocity field (with superimposed streamlines) for a dilute PEO solution in the OSCER at a superficial flow velocity $U = 0.08$ m s^{-1}, Wi $= 0.56$. (b) Velocity field for flow of the same PEO solution at $U = 0.4$ m s^{-1}, Wi $= 2.25$. (c) Dimensionless measured velocity profiles along the $y = 0$ (outflow) axis for the dilute PEO solution over a range of flow rates, along with the Newtonian result. (d) Extension rate as a function of the flow velocity in the OSCER for the dilute PEO solution, also showing the corresponding Newtonian result for comparison.

FIG 3. (a)-(d) Birefringence images of the dilute PEO solution in the OSCER over a range of flow rates. (e) Retardation profiles $R(y)$ across the birefringent strands (along $x = 0$). Insert shows the full-width at half-maximum as a function of Wi, fitted with an equation of the form predicted by Becherer et al. [24]. (f) Intensity profiles along the length of the birefringent strands ($y = 0$), legend as for Fig. 3(e). (g) Peak birefringence intensity as a function of the extension rate, compared with the prediction of the FENE-CR model. The insert shows the ensemble-averaged extension ratio (β) as a function of Wi.

FIG 4. (a) Pressure drop measured in shear (ΔP_{shear}) and extension (ΔP_{total}) for flow of the dilute PEO solution in the OSCER. The insert shows the excess pressure drop ($\Delta P_{excess} = \Delta P_{total} - \Delta P_{shear}$) as a function of $\dot{\varepsilon}$. (b) Extensional viscosity and Trouton ratio as a function of $\dot{\varepsilon}$, determined from both bulk excess pressure drop and local birefringence measurements and compared with the prediction of the FENE-CR model. The insert plot shows Δn versus ΔP_{excess}, used to determine the stress optical coefficient ($C = 0.44 \times 10^{-9}$ Pa^{-1}).

(a)
y
R
x
$2H$
s
→ inflow
→ outflow
s stag. point

(b) $\dot{\varepsilon}_{xx}/(U/H)$
0.1
0
-0.1

(c) N_1 (Pa)
2000
1500
1000
500
0
-500
-1000

(d)
500 μm

Figure 1   LS12897   26JUL2012

Figure 2   LS12897   26JUL2012

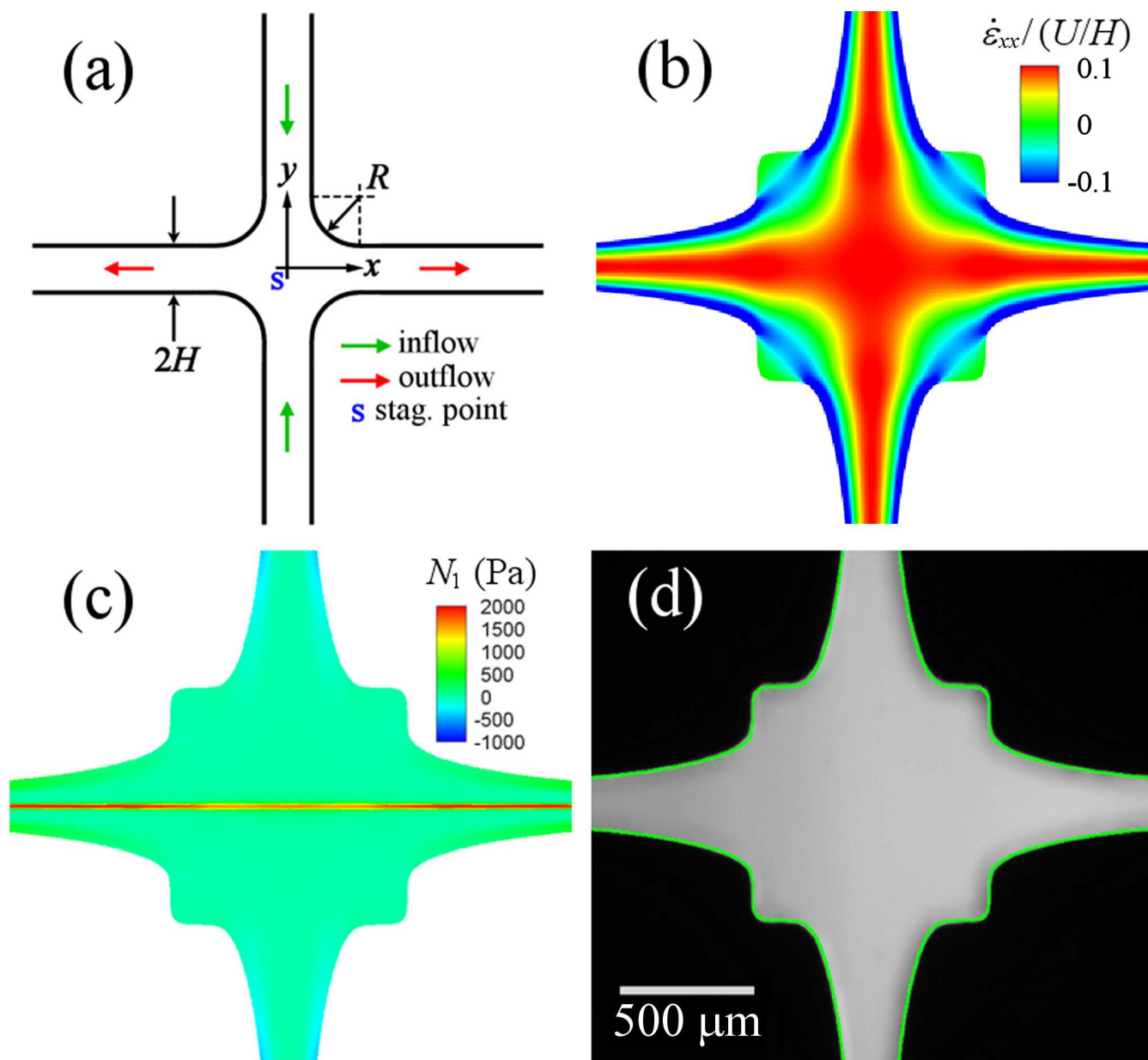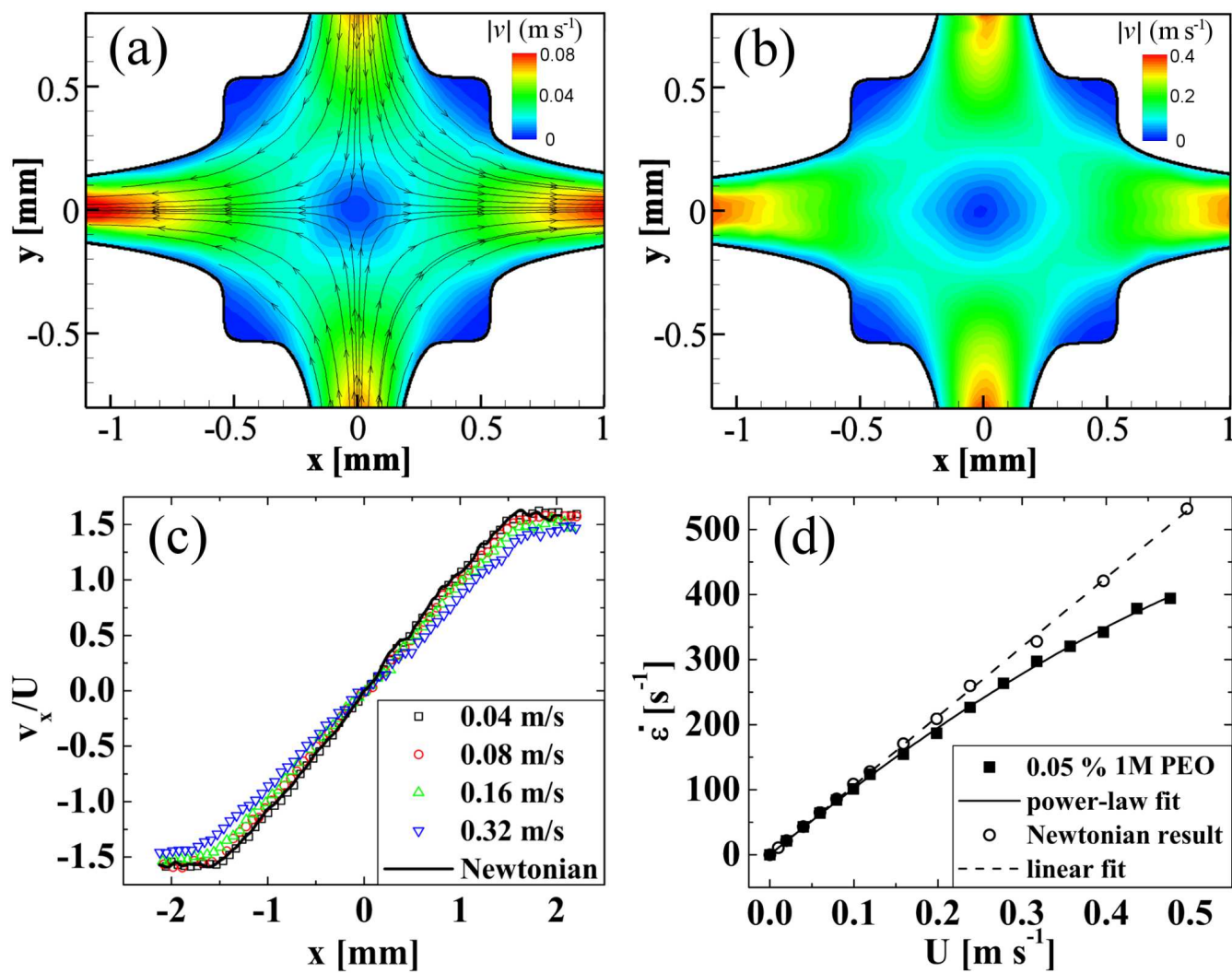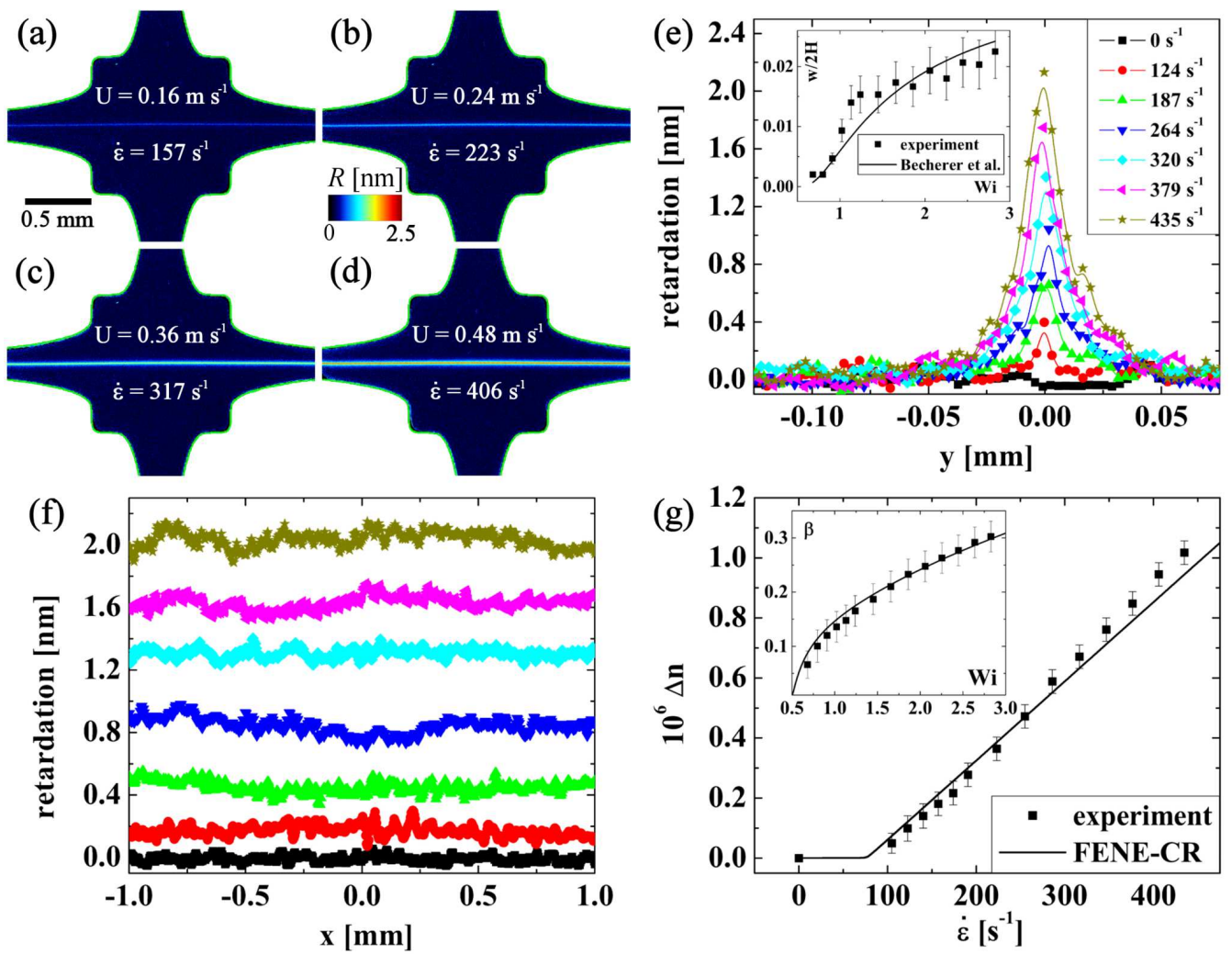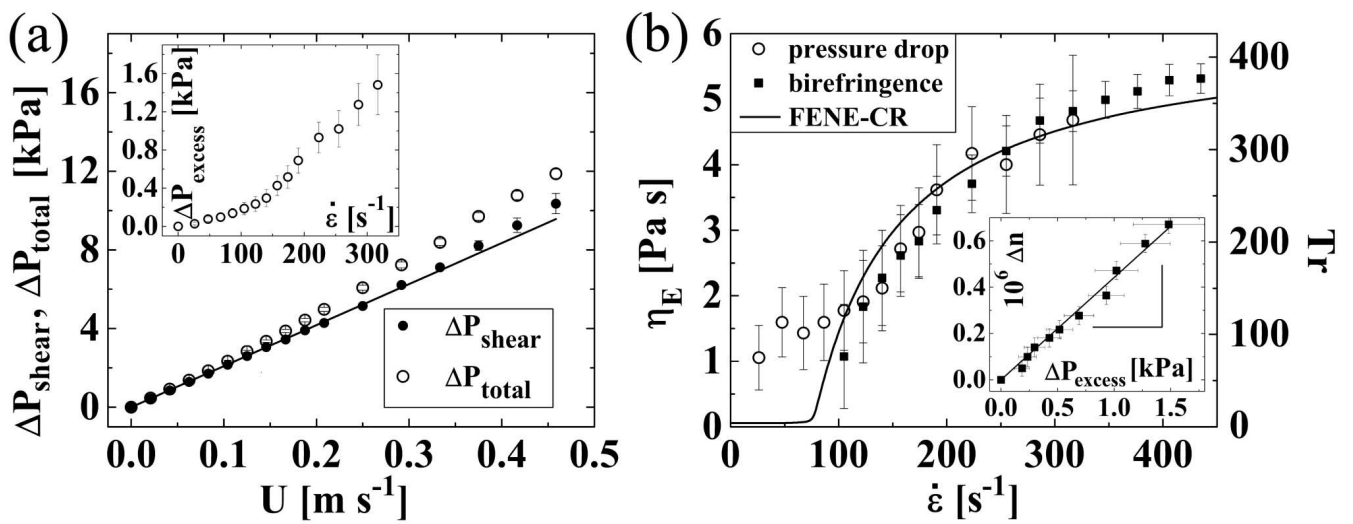Figure 3   LS12897   26JUL2012

Figure 4   LS12897   26JUL2012